Nano Research

Open Access

Research Article

Cathodic corrosion as a facile and universal method for scalable preparation of dual-atom electrocatalysts

Rui Li[1], Tao Shao[2], Fudong Jiang[1], Dong Chen[1], Wenyong Jing[1], Jingwen Ba[1], Yulong Li[1], Yuhan Wu[1], Wenhua Luo[1], and Jingsong Xu[2] ✉

[1] *Institute of Materials, China Academy of Engineering Physics, Mianyang 621907, China*
[2] *Science and Technology on Surface Physics and Chemistry Laboratory, Mianyang 621908, China*

Cite this article: *Nano Research*, **2025**, *18*, 94907264. https://doi.org/10.26599/NR.2025.94907264

ABSTRACT: Dual-atom catalysts (DACs) are emerging as highly efficient electrocatalysts, offering synergistic effects and high atomic utilization. Here, we introduce a scalable and facile electrochemical approach for the top-down synthesis of DACs supported on carbon materials via a two-time "plasma treatment + cathodic corrosion" procedure. Concretely, metal atoms in nanoparticles on cathode are etched under high negative potential, diffused over the electrode, captured by N doped carbon carriers in electrolyte and forming single-atom sites. After introducing additional N coordination sites adjacent to the primary metal single-atom sites via a secondary plasma processing and anchoring a second metal atom via a subsequent cathodic corrosion process, DACs are achieved. The as-prepared Pt DACs exhibit enhanced catalytic activity toward hydrogen evolution reaction (HER) with a low overpotential of 0.027 V at 10 mA·cm^{-2} and a Tafel slope of 29.9 mV·dec^{-1} as well as high stability. Importantly, the proposed electrochemical top-down synthetic route affords promising potential for scalable production of other homonuclear or heteronuclear DACs on multiple carbon substrates, advancing the practical application of DACs in electrocatalysis.

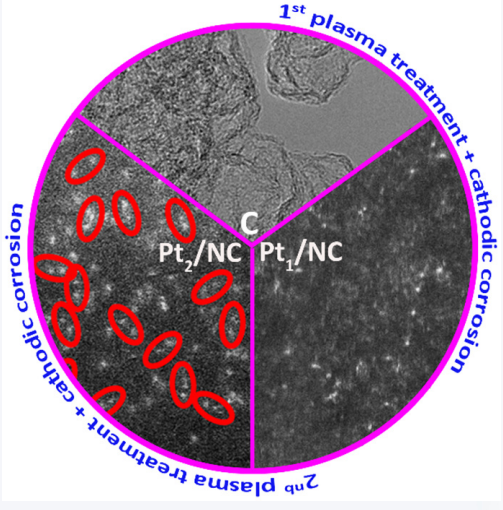

KEYWORDS: dual-atom catalysts, cathodic corrosion, top-down strategy, scalable synthesis, hydrogen evolution reaction

1 Introduction

Dual-atom catalysts (DACs), an extension of single-atom catalysts (SACs), are emerging as a transformative solution in the realm of catalysis, offering new opportunities for the development of highly active catalysts and the investigation of catalytic mechanism [1–3]. Remarkably, DACs not only inherit the high atom efficiency of SACs, but also overcome the limitations of lacking tunable electronic structures for electron redistribution and active sites to adsorb necessary reaction intermediates for complex reactions [4–8]. Their unique structural configuration, where two metal atoms are in pairs and isolated from other metal atoms, provides a platform for unprecedented control over the electronic structure and the synergistic interaction to break the linear scaling relationships between adsorption energies of reaction intermediates [9–13]. Despite the superiority of DACs, the chemical synthesis of DACs, requiring metal atoms keeping arranged in pairs but not monodispersed or aggregated, is much more challenging than that of SACs.

Currently, the preparation of atomic catalysts can be approached through two primary categories of synthetic routes, including bottom-up (e.g. atomic layer deposition and wet-chemistry method) and top-down (e.g. ball milling, abrasion, and atom trapping) strategies [12, 14–18]. Generally, in comparison with bottom-up methods, top-down strategies converting bulk metal or larger metal nanoparticles (NPs) into paired metal atoms by extra energy (e.g. thermal, mechanism, etc.), can minimize waste generation, economize material costs and be more compatible with large-scale manufacturing processes [19, 20]. Typically, a top-down synthetic route first requires volatilizing metal NPs or bulk metals to produce mobile metal atoms by high-temperature emitting or applying mechanochemical abrasion; subsequently, the generated migrating metal atoms are captured by predesigned defects or heteroatom dopants sites of substrates [21, 22]. As for the

Received: November 19, 2024; **Revised:** January 10, 2025
Accepted: January 20, 2025

✉Address correspondence to xjs@caep.cn

fabrication of DACs, a predesigned defect site adjacent to a primary metal single atom is generally demanded to guide the selective anchoring of the mobile metal atom [23–25]. For instance, Zhou et al. reported a top-down synthetic route for Rh-Fe DACs by converting Fe NPs to single atoms adjacent to Ru sites using Rh–Fe bonding as a chemical facilitator [26]. Regretfully, during the process of disrupting the metal–metal bonds for mostly reported top-down strategies, high temperature or stringent mechanochemical treatment are nondeductible, which not only involves complex operation but also results in high energy consumption. Therefore, it is exigent to develop a moderate, environmentally friendly, and cost-effective strategy to synthesize DACs for advancing their further applications.

Cathodic corrosion is an intriguing electrochemical process where metallic cathodes are etched under ultrahigh negative potential in aqueous environment or organic solution [27–29]. The process involves the formation of metastable cation-stabilized metal ions (Zintl-type phase), the diffusion of these metal ions over the electrode, and their following oxidation by the applied solvent [30–33]. Cathodic corrosion strategy has been utilized to prepare metal nanoparticles or nanoalloys from bulk metal or their alloys (e.g. Pt, Au, Ag, PtPd alloy, etc.) [34–37]. Recently, we proposed the feasibility of cathodic corrosion routes to *in-situ* convert metal NPs on cathode into SACs or obtain SACs supported on powdery supports [38, 39]. However, the application of cathodic corrosion strategy to synthesize supported DACs has never been reported.

In this study, we propose a consecutive "plasma treatment + cathodic corrosion" strategy for facile and scalable synthesis of DACs supported on carbon powder. During the cathodic corrosion procedure, Pt atoms are sequentially deposited and captured by the anchoring N dopant sites of carbon materials introduced by plasma treatment. The dominant existence of Pt SACs and DACs after one-time and two-time "plasma treatment + cathodic corrosion" treatment is confirmed by high-angle annular dark-field scanning transmission electron microscopy (HAADF-STEM) and X-ray absorption fine structure (XAFS). The resulted Pt DACs exhibit a high catalytic activity toward hydrogen evolution reaction (HER) with a low overpotential of 0.027 V at 10 mA·cm^{-2} and a Tafel slope of 29.9 mV·dec^{-1}, superior to Pt SACs or NPs. More importantly, the proposed strategy is also promising to fabricate other metal DACs (e.g. Pd_2, Pt_1Pd_1) on other carriers by simply exchanging the applied precursor.

2 Experimental

2.1 Preparation of NC carriers

The synthesis of nitrogen doped carbon black (NC) was achieved through N_2 plasma treatment of commercial carbon black (CB) from XFNano Inc utilizing the LED-2000 apparatus (Chengdu Tongchuang Inc). The plasma treatment was conducted at a voltage of 20 kV for 30 min. With the same operation condition, carbon nanotubes were also converted to N doped carbon nanotubes (NCNT).

2.2 Preparation of Pt SACs

Pt NPs were firstly electrodeposited onto carbon paper (CP, 4 cm × 2.5 cm) by potentiostatic deposition technique at −0.3 V for 600 s using 10 mM H_2PtCl_6 and 0.1 M KCl as electrolyte. Larger CP pieces (10 cm × 5 cm) were used for large-scale fabrication. Similarly, Pd NPs/CP electrode was prepared by replacing H_2PtCl_6 with $PdCl_2$.

The cathodic corrosion procedure was carried out in an alkaline medium containing 5.0 M KOH and 10 mg·mL^{-1} of NC powders. The as-prepared Pt NPs/CP were used as working electrode, while graphite rod and Hg/HgO electrodes were used as counter and reference electrodes, respectively. The Pt NPs/CP electrode was subjected to a high negative potential of −5 V for 30 min with continuous stirring the electrolyte to obtain Pt_1/NC powders.

2.3 Preparation of Pt-based DACs

Pt_1/NC powders were further treated by N_2 plasma at a voltage of 20 kV for 15 min. A secondary cathodic corrosion process was performed in the same electrochemical system except exchanging NC by the plasma treated Pt_1/NC powders. The resulted Pt_2/NC powders were centrifuged and washed by deionized water.

Similarly, Pt_2/NCNT was prepared by exchanging NC by NCNT in the repeated plasma treatment and cathodic corrosion process. Pd_2/NC and Pt_1Pd_1/NC were prepared by replacing Pt NPs/CP with Pd NPs/CP in both or only the secondary cathodic corrosion procedure.

2.4 Characterization

Field emission scanning electron microscopy (SEM) images were obtained by Sirion-200 to investigate the morphologies of Pt NPs/CP. Transmission electron microscopy (TEM) images were recorded by Tecnai F20. HAADF-STEM images were acquired by G280-300 ChemiSTEM at 300 kV. The crystalline phases were characterized by X-ray diffraction (XRD, Y-2000 X-ray diffractometer) with Cu Kα radiation (λ = 0.15418 nm). Raman spectra and X-ray photoelectron spectra (XPS) were collected on Almega XR Raman microscopy with a 532 nm laser and PHI 5000 XPS system with an Al Kα X-ray source (1486.6 eV photons). The mass ratio of Pt was measured by inductively coupled plasma-mass spectrometry (ICP-MS, NexION350). The XAFS was recorded on the beamline BL01C1 in NSRRC supported by Ceshigo Research Service.

2.5 Electrochemical tests

For HER measurement, 4 mg of Pt_1/NC, Pt NPs/NC, or commercial Pt/C catalysts were dispersed and sonicated in a mixed solution containing 40 μL of 5 wt.% Nafion, 480 μL of water, and 480 μL of ethanol to obtain a homogeneous ink. Thereafter, 5 μL of catalysts ink was drop-cast on glassy carbon electrode with a diameter of 5 mm. The electrochemical tests were conducted on CHI 760D electrochemical workstation with an H-type cell. Graphite rod, Ag/AgCl electrode, and N_2-saturated 0.5 M H_2SO_4 solution were used as the counter electrode, reference electrode, and electrolyte, respectively. The linear sweep voltammetry (LSV) was performed at a scan rate of 1 mV·s^{-1}. Electrochemical impedance spectra (EIS) were recorded in the frequency range of 10^6 to 0.1 Hz at an overpotential of 0.1 V. For the accelerated durability tests (ADT), LSV curves were collected after 20,000 cyclic voltammetry (CV) cycles in the potential range from 0.4 to −0.15 V (vs. normal hydrogen electrode (RHE)). Chronoamperometry measurements were conducted at −0.1 V for 100 h.

3 Results and discussion

3.1 Preparation and characterization of DACs

The synthetic procedure of Pt_2/NC through our proposed consecutive "plasma treatment + cathodic corrosion" strategy is

depicted in Fig. 1(a). Initially, Pt NPs were electrodeposited onto commercial CP to serve as the metallic precursor and taken as the working electrode during cathodic corrosion procedure. Meanwhile, commercial CB was conducted by high-energy N_2 plasma treatment for 30 min. During the plasma bombardment, carbon defects and N dopants were introduced in graphitic layer, and NC carriers were thus obtained (Fig. S1 in the Electronic Supplementary Material (ESM)). The as-obtained Pt NPs/CP electrode was then subjected to a high cathodic potential of −5 V in the 5 M KOH solution containing NC carriers for 30 min. During this cathodic corrosion procedure, Pt atoms in Pt NPs were etched, peeled off the electrode and ultimately captured by N anchoring sites of NC carriers, thus obtaining Pt single atoms/NC (Pt_1/NC) catalysts. The as-obtained Pt_1/NC catalysts were separated from the electrolyte and dried for subsequent plasma treatment to introduce additional nitrogen dopants and carbon defects adjacent to the pre-anchored Pt-atom sites. Finally, the plasma treated Pt_1/NC powders were redispersed in 5 M KOH solution as carbon carrier to secondly capture Pt atoms cathodically corroded from Pt NPs/CP, yielding NC supported Pt DACs (Pt_2/NC) products.

Pt NPs were loaded on CP via a potentiostatic deposition technique at −0.3 V in a solution containing 10 mM H_2PtCl_6 and 0.1 M KCl (Fig. S2(a) in the ESM). As shown in Figs. S2(b) and S2(c) in the ESM, Pt NPs with a diameter of about 400 nm were anchored on the smooth surface of carbon fibers of CP. A three-electrode system was established for further cathodic corrosion with the as-obtained Pt NPs/CP electrode, graphite rod, and Hg/HgO electrode as the working electrode, counter electrode, and reference electrode, respectively. A high-concentration alkaline solution of 5 M KOH was used to stabilize the metastable atomic Pt anions produced during cathodic corrosion procedure. 10 mg·mL^{-1} of plasma treated NC powders was also dispersed in the electrolyte to capture the dispersed Pt atoms during cathodic corrosion process. After applying direct current at −5 V for 30 min, large Pt NPs on CP were transformed to smaller ones with a size of about 50 nm, indicating the successful etching, diffusion, and recombination of Pt atoms in Pt NPs (Fig. S3 in the ESM). Meanwhile, HAADF-STEM images indicate the formation of uniformly dispersed Pt single atoms on NC without existence of visible clusters or NPs (Fig. 1(b) and Fig. S4(a) in the ESM). The uniform distribution of Pt elements was further confirmed by energy dispersive X-ray spectroscopy (EDS) mapping analysis at a large scale (Fig. S5 in the ESM). The loading amount of Pt in Pt_1/NC was determined to be 4.3% according to the ICP-MS analysis. The Pt_1/NC powders were centrifuged, washed, dried, treated by N_2 plasma and utilized as powdery carriers for the second time. After the same cathodic corrosion process in 5 M KOH solution at −5 V for 15 min, some pairwise bright dots (marked with red circles) were observed in STEM image (Fig. S6 in the ESM). After cathodic corrosion for 30 min, more atomic pairs were observed, suggesting the successful formation of Pt_2 dimers (Fig. 1(c)). As expected, no larger particles were observed in TEM images (Fig. S4(b) in the ESM). Through analyzing 50 Pt pairs, the distances between neighboring Pt atoms were determined to be 2.4 to 3.3 Å (Fig. S7 in the ESM). The different interatomic distance is perhaps due to the different direction of Pt pairs relative to the incident beam direction. Some isolated bright dots (marked with white circles) were also observed, probably attributed to the individual Pt atom impurity and destroyed Pt_2 dimers under high-energy or prolonged electron beam. Pt atoms remained uniformly dispersed on NC according to EDS mapping results (Fig. S8 in the ESM). ICP-MS suggested a larger mass ratio of 7.7% for Pt in Pt_2/NC, indicating additional loading during the subsequent cathodic corrosion process. Notably, the subsequent N_2 plasma treatment is also necessary for the synthesis of Pt DACs. Solely prolonging the duration time of the first N_2 plasma treatment and cathodic corrosion process will lead to the formation of Pt clusters due to the lack of suitable anchoring sites for dissociative Pt atoms (Fig. S9 in the ESM).

The compositional and structural changes during the synthetic process were characterized by multiple techniques. As shown in the XRD patterns, all samples including CB, NC, Pt_1/NC, and Pt_2/NC exhibit a dominant peak at about 22.8° corresponding to (002) planes of graphite, indicating the retained graphitic structure in the core carbon powders after N_2 plasma treatment and cathodic corrosion procedure (Fig. S10(a) in the ESM). No characteristic signals of Pt crystalline (JCPDS No. 04-0802) were observed in Pt_1/NC and Pt_2/NC, suggesting the uniform dispersion of Pt single atoms or dimers. The Raman spectra are depicted in Fig. S10(b) in the ESM. CB shows an intense peak at 1582 cm^{-1} ascribed to graphitic carbon (G-band) and a weak peak at 1340 cm^{-1} ascribed to

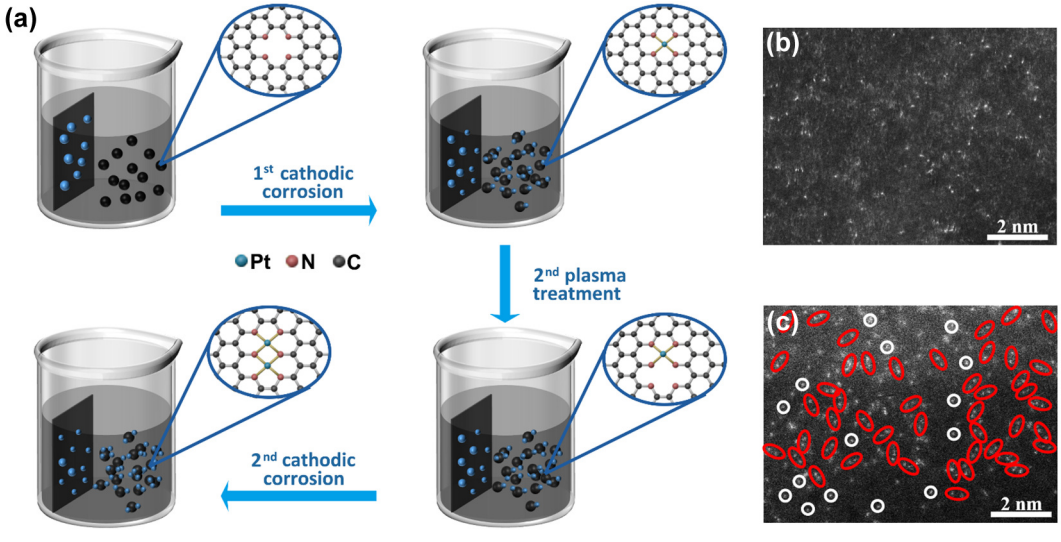

Figure 1 (a) Schematic illustration of preparation of Pt_2/NC by "plasma treatment + cathodic corrosion" method. HAADF-STEM images of (b) Pt_1/NC and (c) Pt_2/NC obtained after one and two cycle of "plasma treatment + cathodic corrosion".

defects/disorders (D-band) with an intensity ratio (I_D/I_G) of 0.19, suggesting nearly entire graphitic structure for CB [40]. The D and G peaks became much broader and the I_D/I_G turned to 0.83 after N_2 plasma bombardment, demonstrating the successful introduction of N dopants and carbon defects in the surficial area of NC. After cathodic corrosion induced Pt deposition, Pt_1/NC exhibited a lower I_D/I_G of 0.82 due to the partial removal of oxygen containing groups at high negative potential. Similarly, after another cycle of introduction of N and O dopants and carbon defects during plasma treatment and partial reduction of oxidized groups during cathodic corrosion process, Pt_2/NC exhibited a slightly increased I_D/I_G of 0.87. XPS analysis was further performed to investigate the elemental composition and chemical states of all samples. As shown in Fig. S11 in the ESM, CB exhibits a strong signal corresponding to C element and negligible signals for N and O elements. As a comparison, NC shows three main peaks at 285, 533, and 400 eV ascribed to C, O, and N elements, and the atom ratios of C, N, and O are calculated to be 84.7 at.%, 7.6 at.%, and 7.7 at.%, respectively (Fig. S12(a) in the ESM). C elements were in the forms of C–C/C=C, C–N/C–O, and C=O, exhibiting corresponding peaks at 284.4, 285.9, and 288.8 eV (Fig. S12(b) in the ESM) [41]. The high-resolution N 1s spectrum was deconvoluted into pyridinic N (398.3 eV), pyrrolic N (400.1 eV), and graphitic N (401.1 eV) species, indicating the successful introduction of N dopants by plasma treatment (Fig. 2(a)) [41, 42]. Moreover, O containing species, including C–O (533.6 eV) and C=O (532.4 eV) bonds, are formed by oxidation of surficial carbon defects when carbon powders encountering air after plasma bombardment (Fig. S12(c) in the ESM) [43]. After cathodic corrosion procedure, Pt_1/NC exhibits obvious signals of C, N, O, and Pt elements (Fig. S13 in the ESM). Compared with NC precursor, high-resolution N 1s spectrum of Pt_1/NC shows a much stronger peak at 398.3 eV, illustrating the existence of Pt–N bonds (Fig. 2(a)) [44, 45]. Pt 4f peaks are observed at binding energies of 72.9 and 76.1 eV, higher than those of commercial Pt/C (71.6 and 74.8 eV), demonstrating a higher oxidation state of Pt in Pt_1/NC (Fig. 2(b)). Subsequent plasma treatment and cathodic corrosion process lead to more carbon defects with stronger peaks for C–N/C–O and additional introduction of N dopants with an atom ratio of 8.7% (Fig. S14 in the ESM). Meanwhile, stronger signals for Pt–N bonds were observed in N 1s spectrum, suggesting larger loading amount of Pt on N sites (Fig. 2(a)). Pt 4f peaks exhibit a slight negative shift (72.6 and 75.6 eV) than those of Pt_1/NC, indicating a slightly lower oxidation state of Pt in Pt_2/NC than that in Pt_1/NC (Fig. 2(b)) [46, 47].

To acquire deeper insights into the electronic structure and coordination environment of Pt atoms in Pt_1/NC and Pt_2/NC, X-ray absorption near edge structure (XANES) and extended X-ray absorption fine structure (EXAFS) were performed. As shown in Fig. 2(c), Pt_1/NC exhibits white line intensity between that of Pt foil and PtO_2, illustrating a positive charge and partial oxidation of Pt atoms, in accordance with XPS results. Meanwhile, Pt_1/NC shows a prominent peak at 1.60 Å ascribed to Pt–N/C coordination whereas no characteristic signals corresponding to Pt–Pt contributions at 2.58 Å in the Fourier transformed EXAFS spectrum, suggesting inexistence of Pt NPs or clusters (Fig. 2(d)). The fitting results further confirm the sole existence of Pt–N/C bonds and the coordination number is determined to be 3.9 (Fig. 2(e) and Table S1 in the ESM). After subsequent deposition of another Pt atom by secondary plasma treatment and cathodic corrosion procedure, Pt_2/NC also exhibits white line intensity between those of Pt foil and PtO_2, indicating the positive charge of Pt atoms due to the strong interaction between Pt_2 dimers and the substrate. The EXAFS spectrum of Pt_2/NC retains the strong peak at 1.60 Å, suggesting the reservation of Pt–N/C bonds. Another peak is found at higher R value of 2.45 Å, corresponding to the formation of Pt dimers. According to the fitting results, the average coordination numbers of Pt–N/C and Pt–Pt are 3.9 and 0.8, respectively (Fig. 2(f) and Table S1 in the ESM). Notably, carbon defects, nitrogen dopants, and oxygen dopants are all introduced into NC carrier during plasma treatment, it is thus deduced that the contributions of Pt–N, Pt–C, and even Pt–O coexist. And it is hard to distinguish them due to the similar characteristic peak of these bonds.

The above characterization results confirm the successful top-

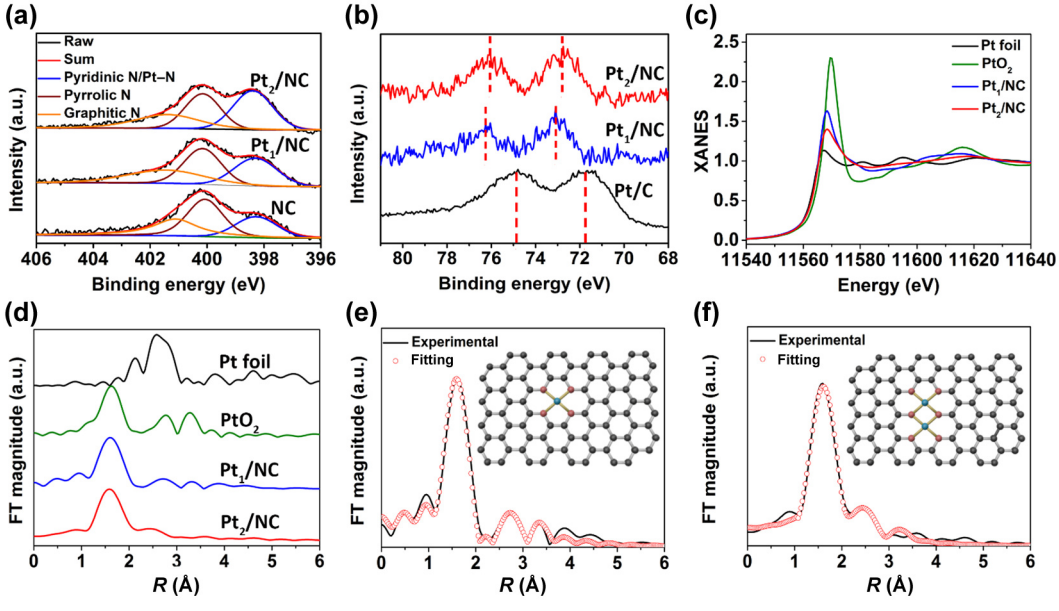

Figure 2 High-resolution (a) N 2p XPS spectra of Pt_2/NC, Pt_1/NC, and NC. (b) Pt 4f XPS spectra of Pt_2/NC, Pt_1/NC, and Pt/C. (c) XANES spectra at the Pt L_3-edge and (d) Fourier transform of EXAFS spectra of Pt foil, PtO_2, Pt_1/NC, and Pt_2/NC. R-space fitting curves for (e) Pt_1/NC and (f) Pt_2/NC.

down synthesis of Pt DACs by the proposed consecutive "plasma treatment + cathodic corrosion" strategy. In consideration of the mechanism of cathodic corrosion and sequential deposition strategy for synthesizing DACs, the formation mechanism of Pt_2 dimers is as follows. During N_2 plasma processing, high-energy ions collide with the surface of carbon powders and cause physical sputtering, creating vacancies and defects in the carbon lattice [48, 49]. Meanwhile, reactive nitrogen atoms or ions react with the carbon species and replace some carbon atoms, resulting in N dopants sites in NC. When subjected to high negative potential, Pt bonds in Pt NPs/CP electrode decompose and metal anions stabilized by alkaline ions are formed [50, 51]. In aqueous media, when these diffused Pt anions surpass the water-free region near the cathode and encounter water molecules, they are quickly reoxidized to metal atoms, either redepositing on the electrode to form smaller NPs or captured by N dopant sites on NC in the electrolyte to form Pt_1/NC [30, 52]. During subsequent N_2 plasma processing, volatile CN species are formed and sputtered again, leaving isolated Pt atoms and introducing fresh carbon defects and N dopants sites on Pt_1/NC powders. Within subsequent cathodic corrosion procedure, Pt atoms detached from Pt NPs/CP are further captured by these plasma-treated Pt_1/NC powders. Since the binding energy of Pt atoms on vacancies adjacent to preformed Pt SACs (Pt_1-N_6G) is higher to that on pure nitrogen dopant sites (N_4G), Pt_2 dimers are preferentially formed [53].

According to above mechanism, it is deduced that the proposed synthetic route is promising to prepare other supported metal DACs by taking corresponding metals and carbon materials as the precursors. As reported, cathodic corrosion phenomenon appears for various metals whose anions can be stabilized in the form of Zintl phase, such as Pt, Au, Pd, Ir, Cu, Rh, Bi, and Ru [27, 30, 34]. Therefore, we used Pd NPs/CP as metal precursor and obtained uniformly dispersed Pd dimers with an average distance of 2.63 Å on NC carriers (Fig. 3(a) and Fig. S15(a) in the ESM). TEM and XRD results excluded the existence of crystalline Pd species (Figs. S15(b) and S15(c) in the ESM), and XPS results suggested the formation of Pd–N bonds (Fig. S16 in the ESM). Notably, since the secondary metal atom is deposited adjacent to the preformed one in an individual process, this strategy is also suitable to prepare heteronuclear DACs by applying two different metal precursors. Here, we took Pt NPs/CP and Pd NPs/CP as metal resources in the initial and subsequent cathodic corrosion procedure respectively and successfully obtained Pt_1Pd_1/NC catalysts (Fig. 3(b) and Fig. S17 in the ESM). The carbon carriers can also be replaced by applying other carbon precursors or conducting different kinds of plasma. For example, we replaced NC carriers by NCNT powders and obtained Pt_2/NCNT catalysts (Fig. 3(c) and Fig. S18 in the ESM). Moreover, the synthesis of metal DACs by consecutive "plasma treatment + cathodic corrosion" strategy can be facilely scaled up. Through applying larger electrolytic cell and more NC precursors, we prepared 2 g of Pt_2/NC catalysts with the same synthetic procedure (Fig. S19(a) in the ESM). As expected, Pt_2 dimers are observed in STEM images without larger clusters or NPs and the loading amount of Pt is determined to be 7.2% (Fig. 3(d) and Figs. S19(b)–S19(d) in the ESM).

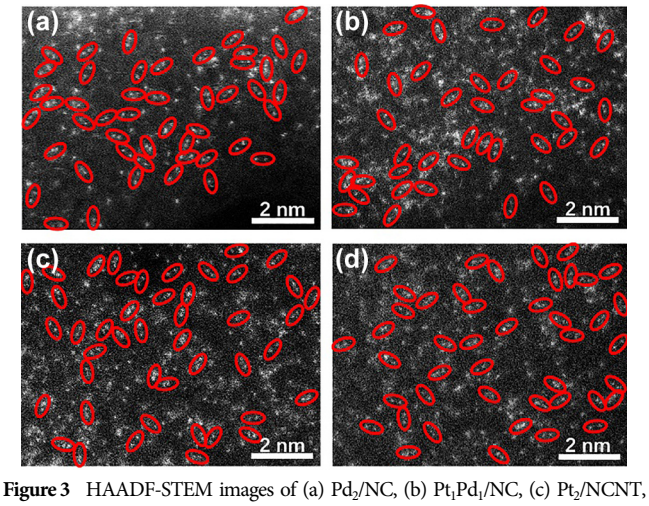

Figure 3 HAADF-STEM images of (a) Pd_2/NC, (b) Pt_1Pd_1/NC, (c) Pt_2/NCNT, and (d) Pt_2/NC with large-scale preparation.

3.2 Catalytic properties toward HER

Electrocatalytic HER is a pivotal process in electrochemical energy conversion [54–56], and here we choose HER as a model reaction to study the influence of catalytic activity by adding another Pt atom adjacent to the Pt SACs. Figure 4(a) depicts the polarization curves of as-prepared Pt_2/NC, Pt_1/NC, NC carriers, and commercial Pt/C counterpart recorded by LSV technique in N_2-saturated 0.5 M H_2SO_4 solution with a standard three-electrode system. NC carriers show poor catalytic activity, while Pt_2/NC presents superior activity with a low overpotential of 0.027 V at 10 mA·cm^{-2}, which is better than that of Pt_1/NC (0.034 V), Pt/C counterpart (0.051 V), and Pt clusters/NC catalysts with higher Pt content prepared by a prolonged N_2 plasma treatment and cathodic corrosion process (0.036 V, Fig. S20 in the ESM) and comparable with other Pt-based dual-atom HER catalysts (Table S2 in the ESM) [57–63]. Similarly, Pt_2/NC exhibited higher activity when corrected by electrochemical active surface area (ECSA) (Fig. S21 in the ESM). The higher catalytic activity of Pt_2/NC is probably due to the higher loading amount of Pt atoms and the interaction between Pt dimers. Notably, Pt_2/NC prepared with 2 g of NC precursor also exhibited a good catalytic activity, indicating the feasibility of large-scale synthesis of DACs by the proposed method (Fig. S22 in the ESM). The mass activities of Pt_2/NC, Pt_1/NC, and Pt/C are further calculated to be 31.5, 21.4, and 1.6 A·mg^{-1} at an overpoential of 0.1 V, demonstrating the enhancement of HER activity by formation of Pt_2 dimers in contrast to isolated single atoms or larger NPs (Fig. 4(b)). Assuming all Pt atoms were available, the turnover frequency of Pt_2/NC at −0.1 and −0.2 V are calculated to be 31.3 and 849.7 s^{-1}.

The Tafel slopes were also recorded in Fig. 4(c). Pt_2/NC exhibits a Tafel slope of 29.9 mV·dec^{-1}, smaller than those of Pt_1/NC (34.6 mV·dec^{-1}) and Pt/C (33.3 mV·dec^{-1}), indicating Tafel step as the rate-limiting step [64]. EIS measurements were performed from 100 kHz to 1 Hz to investigate the kinetics of HER on different catalysts. As shown in Fig. S23 in the ESM, the solution resistances (R_s) are about 0.49 Ω·cm^2 for all catalysts, while Pt_2/NC exhibits a smaller charge transfer resistance (R_{ct}) of 3.8 Ω·cm^2 than those of Pt_1/NC (9.2 Ω·cm^2) and Pt/C counterparts (16.1 Ω·cm^2), further suggesting the faster HRE kinetics of Pt_2 dimers. The durability of Pt_2/NC, Pt_1/NC, and commercial Pt/C counterpart were evaluated by ADTs for 20,000 cyclic voltammetry sweeps. As shown in Fig. 4(d), the polarization curve of Pt_2/NC exhibits negligible changes after ADT tests with only 4.3% loss of catalytic activity at an overpotential of 0.05 V. Due to the strong interaction between Pt atoms and N dopants, Pt_1/NC also shows similar catalytic performance as the initial test after ADT tests with 8.2% current

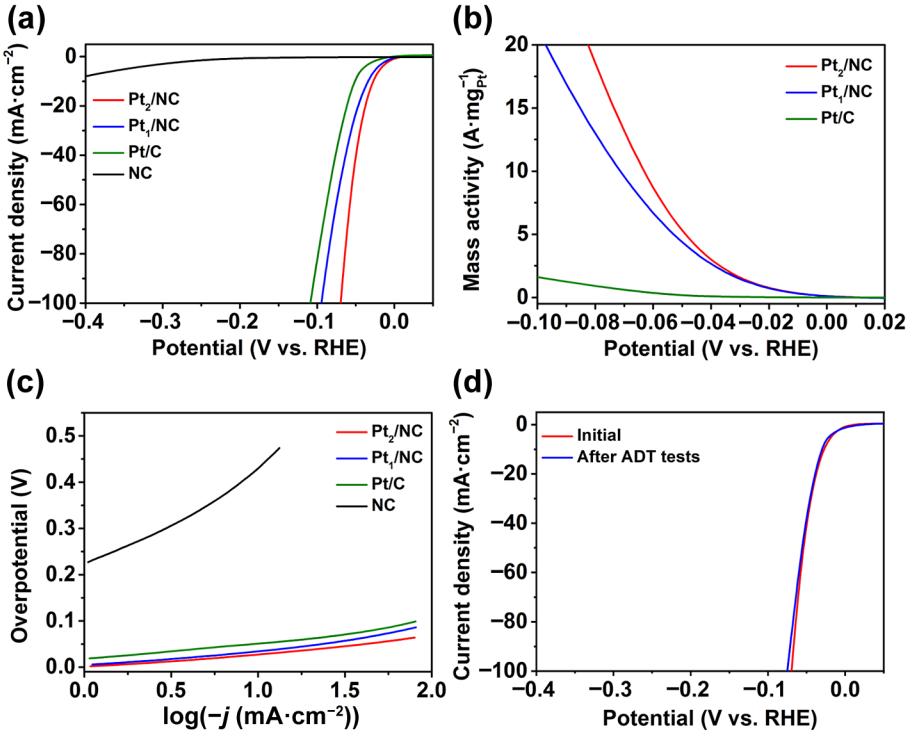

Figure 4 (a) HER polarization curves, (b) mass activities, and (c) Tafel plots of Pt_2/NC, Pt_1/NC, Pt/C, and NC catalysts. (d) Polarization curves of Pt_2/NC before and after ADT for 20,000 CV cycles.

loss at −0.05 V (Fig. S24(a) in the ESM), whereas the activity of Pt/C decreases 27.5% at an overpotential of 0.05 V, indicating a poor stability (Fig. S24(b) in the ESM). The stability of Pt_2 dimers was further confirmed by STEM images of post-testing Pt_2/NC samples (Fig. S25 in the ESM). The chemical valences of Pt elements also exhibited no visible changes as viewed in XPS spectra and no Pt crystals were observed in XRD pattern (Fig. S26 in the ESM). The galvanostatic measurements were also carried out to test the long-term stability of Pt DACs and Pt SACs. After conducting at an overpotential of −0.1 V for 100 h, Pt_2/NC and Pt_1/NC exhibit only 2.5% and 1.1% current loss, superior to that of Pt/C catalysts (33.6%) (Fig. S27 in the ESM).

4 Conclusions

In summary, we proposed a facile and scalable "plasma treatment + cathodic corrosion" route for top-down synthesis of metal DACs. The formation of pairwise metal atoms is well confirmed by STEM and XAFS. The as-prepared Pt_2/NC catalyst exhibits good catalytic activity toward HER with a low overpotential of 0.027 V at 10 mA·cm^{-2}, a Tafel slope of 29.9 mV·dec^{-1} as well as a long-term stability. The proposed synthetic method can be expanded to fabricate other homonuclear or heteronuclear DACs on multiple carbon supports, and promising for large-scale synthesis. This work highlights a promising and universal strategy for scalable top-down synthesis of supported metal DACs without involvement of harsh conditions, benefiting their development and application.

Electronic Supplementary Material: Supplementary material (TEM, EDX and XPS of Pt_1/NC and Pt_2/NC; stability tests of Pt_2/NC) is available in the online version of this article at https://doi.org/10.26599/NR.2025.94907264.

Data availability

All data needed to support the conclusions in the paper are presented in the manuscript and the Electronic Supplementary Material. Additional data related to this paper may be requested from the corresponding author upon request.

Acknowledgements

This work is financially supported by National MCF Energy Research and Development Program (No. 2022YFE03170004), the National Natural Science Foundation of China (Nos. 22019146, and 22309169), Emei Tianfu Leading Talent Program in Sichuan Province (No. RCQC202201), Sichuan Province Natural Science Foundation Innovation Research Team Program (No. 2024NSFTD0018), and Foundation from Institute of Materials CAEP (No. JBNY060201).

Declaration of competing interest

All the contributing authors report no conflict of interests in this work.

Author contribution statement

R. L.: Formal analysis, funding acquisition, investigation, methodology, writing – original draft. T. S.: Formal analysis, validation, writing – original draft. F. D. J.: Formal analysis. D. C.: Methodology. W. Y. J.: Methodology. J. W. B.: Methodology. Y. L. L.: Formal analysis. Y. H. W.: Methodology. W. H. L.: Writing – review & editing. J. S. X.: Conceptualization; funding acquisition; project administration; resources; writing – review & editing. All the authors have approved the final manuscript.

Use of AI statement

None.

References

[1] Jiang, X. L.; Chen, C.; Chen, J. J.; Yu, S. N.; Yu, W.; Shen, L. G.; Li, B. S.; Zhou, M. Z.; Lin, H. J. Atomically dispersed dual-atom catalysts: A new rising star in environmental remediation. *Sci. Total Environ.* **2024**, *912*, 169142.

[2] Yang, X.; Xu, L. Y.; Li, Y. X. Do we achieve "1+1 > 2" in dual-atom or dual-single-atom catalysts. *Coord. Chem. Rev.* **2024**, *516*, 215961.

[3] Yasin, G.; Kumar, A.; Ajmal, S.; Mushtaq, M. A.; Tabish, M.; Saad, A.; Assiri, M. A.; Nazir, M. T.; Zhuo, Q. F. Advances and perspectives on heteronuclear dual-atomic catalysts for prevailing the linear scaling relationship in electrocatalytic CO_2 reduction. *Coord. Chem. Rev.* **2024**, *501*, 215589.

[4] Yang, J. R.; Zeng, D. Q.; Li, J.; Dong, L. Q.; Ong, W. J.; He, Y. L. A highly efficient Fenton-like catalyst based on isolated diatomic Fe-Co anchored on N-doped porous carbon. *Chem. Eng. J.* **2021**, *404*, 126376.

[5] Xie, Y. H.; Chen, X.; Sun, K. A.; Zhang, J. Q.; Lai, W. H.; Liu, H.; Wang, G. X. Direct oxygen-oxygen cleavage through optimizing interatomic distances in dual single-atom electrocatalysts for efficient oxygen reduction reaction. *Angew. Chem., Int. Ed.* **2023**, *62*, e202301833.

[6] Lei, L.; Guo, X. H.; Han, X.; Fei, L.; Guo, X.; Wang, D. G. From synthesis to mechanisms: In-depth exploration of the dual-atom catalytic mechanisms toward oxygen electrocatalysis. *Adv. Mater.* **2024**, *36*, 2311434.

[7] Liang, M. F.; Shao, X. D.; Lee, H. Recent developments of dual single-atom catalysts for nitrogen reduction reaction. *Chem.—Eur. J.* **2024**, *30*, e202302843.

[8] Roth-Zawadzki, A. M.; Nielsen, A. J.; Tankard, R. E.; Kibsgaard, J. Dual and triple atom electrocatalysts for energy conversion (CO_2RR, NRR, ORR, OER, and HER): Synthesis, characterization, and activity evaluation. *ACS Catal.* **2024**, *14*, 1121–1145.

[9] Zhou, X.; Han, K.; Li, K.; Pan, J.; Wang, X.; Shi, W. D.; Song, S. Y.; Zhang, H. J. Dual-site single-atom catalysts with high performance for three-way catalysis. *Adv. Mater.* **2022**, *34*, 2201859.

[10] Gao, Y.; Liu, B. Z.; Wang, D. S. Microenvironment engineering of single/dual-atom catalysts for electrocatalytic application. *Adv. Mater.* **2023**, *35*, 2209654.

[11] Liu, K. H.; Li, J.; Liu, Y. Y.; Wang, M. R.; Cui, H. T. Dual metal atom catalysts: Advantages in electrocatalytic reactions. *J. Energy Chem.* **2023**, *79*, 515–534.

[12] Pu, T. C.; Ding, J. Q.; Zhang, F. X.; Wang, K.; Cao, N.; Hensen, E. J. M.; Xie, P. F. Dual atom catalysts for energy and environmental applications. *Angew. Chem., Int. Ed.* **2023**, *62*, e202305964.

[13] Zhang, S. L.; Hou, M. C.; Zhai, Y. L.; Liu, H. J.; Zhai, D.; Zhu, Y. Q.; Ma, L.; Wei, B.; Huang, J. Dual-active-sites single-atom catalysts for advanced applications. *Small* **2023**, *19*, 2302739.

[14] Singh, B.; Gawande, M. B.; Kute, A. D.; Varma, R. S.; Fornasiero, P.; McNeice, P.; Jagadeesh, R. V.; Beller, M.; Zbořil, R. Single-atom (iron-based) catalysts: Synthesis and applications. *Chem. Rev.* **2021**, *121*, 13620–13697.

[15] Zhang, J.; Huang, Q. A.; Wang, J.; Wang, J.; Zhang, J. J.; Zhao, Y. F. Supported dual-atom catalysts: Preparation, characterization, and potential applications. *Chin. J. Catal.* **2020**, *41*, 783–798.

[16] Zong, L. B.; Lu, F. H.; Li, P.; Fan, K. C.; Zhan, T. R.; Liu, P. R.; Jiang, L. X.; Chen, D. H.; Zhang, R. Y.; Wang, L. Thermal shock synthesis for loading sub-2 nm Ru nanoclusters on titanium nitride as a remarkable electrocatalyst toward hydrogen evolution reaction. *Adv. Mater.* **2024**, *36*, 2403525.

[17] Zong, L. B.; Fan, K. C.; Cui, L. X.; Lu, F. H.; Liu, P. R.; Li, B.; Feng, S. H.; Wang, L. Constructing Fe-N_4 sites through anion exchange-mediated transformation of Fe coordination environments in hierarchical carbon support for efficient oxygen reduction. *Angew. Chem., Int. Ed.* **2023**, *62*, e202309784.

[18] Chen, Z. J.; Han, N.; Wei, W.; Chu, D. W.; Ni, B. J. Dual doping: An emerging strategy to construct efficient metal catalysts for water electrolysis. *EcoEnergy* **2024**, *2*, 114–140.

[19] Han, G. F.; Li, F.; Rykov, A. I.; Im, Y. K.; Yu, S. Y.; Jeon, J. P.; Kim, S. J.; Zhou, W. H.; Ge, R. L.; Ao, Z. M. et al. Abrading bulk metal into single atoms. *Nat. Nanotechnol.* **2022**, *17*, 403–407.

[20] Matthews, T.; Mashola, T. A.; Adegoke, K. A.; Mugadza, K.; Fakude, C. T.; Adegoke, O. R.; Adekunle, A. S.; Ndungu, P.; Maxakato, N. W. Electrocatalytic activity on single atoms catalysts: Synthesis strategies, characterization, classification, and energy conversion applications. *Coord. Chem. Rev.* **2022**, *467*, 214600.

[21] Wang, H. L.; Wang, X.; Pan, J.; Zhang, L. L.; Zhao, M.; Xu, J.; Liu, B.; Shi, W. D.; Song, S. Y.; Zhang, H. J. Ball-milling induced debonding of surface atoms from metal bulk for construing high-performance dual-site single-atom catalysts. *Angew. Chem., Int. Ed.* **2021**, *60*, 23154–23158.

[22] Pu, T. C.; Ding, J. Q.; Tang, X.; Yang, K. W.; Wang, K.; Huang, B.; Dai, S.; He, Y.; Shi, Y.; Xie, P. F. Rational design of precious-metal single-atom catalysts for methane combustion. *ACS Appl. Mater. Interfaces* **2022**, *14*, 43141–43150.

[23] Chen, H. Y.; Zhang, Y.; He, Q.; Zhang, H.; Xu, S.; He, X. H.; Ji, H. B. A facile route to fabricate double atom catalysts with controllable atomic spacing for the r-WGS reaction. *J. Mater. Chem. A* **2020**, *8*, 2364–2368.

[24] Cui, T. C.; Liu, Q. M.; Chen, S. W. Dual-atom catalysts for electrochemical energy technologies. *Energy Technol.* **2023**, *11*, 2201456.

[25] Ajmal, S.; Zhao, Y. L.; Yasin, G.; Boakye, F. O.; Tabish, M.; Alam, M. M.; Al-Sehemi, A. G.; Zhao, W. Transition metals based dual single-atom catalysts for oxygen electrocatalysis: Stunning advances and future prospects. *ChemCatChem* **2024**, *16*, e202301392.

[26] Zhou, Y.; Song, E. H.; Chen, W.; Segre, C. U.; Zhou, J. D.; Lin, Y. C.; Zhu, C.; Ma, R. G.; Liu, P.; Chu, S. F. et al. Dual-metal interbonding as the chemical facilitator for single-atom dispersions. *Adv. Mater.* **2020**, *32*, 2003484.

[27] Wirtanen, T.; Prenzel, T.; Tessonnier, J. P.; Waldvogel, S. R. Cathodic corrosion of metal electrodes-how to prevent it in electroorganic synthesis. *Chem. Rev.* **2021**, *121*, 10241–10270.

[28] Chen, X. T.; Koper, M. T. M. *In situ* EC-AFM study of the initial stages of cathodic corrosion of Pt(111) and polycrystalline Pt in acid solution. *J. Phys. Chem. Lett.* **2023**, *14*, 4997–5003.

[29] Li, G. P.; Liu, H.; Yang, H.; Chen, X. Y.; Ji, K. M.; Yang, D. C.; Zhang, S.; Ma, X. B. Tuning product distributions of CO_2 electroreduction over copper foil through cathodic corrosion. *Chem. Eng. Sci.* **2022**, *263*, 118142.

[30] Hersbach, T. J. P.; Koper, M. T. M. Cathodic corrosion: 21st century insights into a 19th century phenomenon. *Curr. Opin. Electrochem.* **2021**, *26*, 100653.

[31] Elnagar, M. M.; Kibler, L. A.; Jacob, T. Structural evolution of Au electrodes during cathodic corrosion: Initial stages of octahedral-nanocrystal growth. *J. Electrochem. Soc.* **2022**, *169*, 102509.

[32] Hersbach, T. J. P.; McCrum, I. T.; Anastasiadou, D.; Wever, R.; Calle-Vallejo, F.; Koper, M. T. M. Alkali metal cation effects in structuring Pt, Rh, and Au surfaces through cathodic corrosion. *ACS Appl. Mater. Interfaces* **2018**, *10*, 39363–39379.

[33] Yang, Y.; Shao, Y. T.; Lu, X. Y.; Yang, Y.; Ko, H. Y.; DiStasio, R. A. Jr. ; DiSalvo, F. J.; Muller, D. A.; Abruña, H. D. Elucidating cathodic corrosion mechanisms with operando electrochemical transmission electron microscopy. *J. Am. Chem. Soc.* **2022**, *144*, 15698–15708.

[34] Feng, J. C.; Chen, D.; Sediq, A. S.; Romeijn, S.; Tichelaar, F. D.; Jiskoot, W.; Yang, J.; Koper, M. T. M. Cathodic corrosion of a bulk wire to nonaggregated functional nanocrystals and nanoalloys. *ACS Appl. Mater. Interfaces* **2018**, *10*, 9532–9540.

[35] Vanrenterghem, B.; Bele, M.; Zepeda, F. R.; Šala, M.; Hodnik, N.; Breugelmans, T. Cutting the Gordian Knot of electrodeposition via controlled cathodic corrosion enabling the production of supported metal nanoparticles below 5 nm. *Appl. Catal. B: Environ.* **2018**, *226*, 396–402.

[36] Yanson, A. I.; Rodriguez, P.; Garcia-Araez, N.; Mom, R. V.; Tichelaar, F. D.; Koper, M. T. M. Cathodic corrosion: A quick, clean, and versatile method for the synthesis of metallic nanoparticles. *Angew. Chem., Int. Ed.* **2011**, *50*, 6346–6350.

[37] Yang, Y. C.; Qiao, B. H.; Wu, Z. P.; Ji, X. B. Cathodic corrosion: An electrochemical approach to capture Zintl compounds for powder materials. *J. Mater. Chem. A* **2015**, *3*, 5328–5336.

[38] Li, R.; Xu, J. S.; Zhao, Q. K.; Ren, W. S.; Zeng, R. G.; Pan, Q. F.; Yan, X. Y.; Ba, J. W.; Tang, T.; Luo, W. H. Cathodic corrosion as a facile and universal method for the preparation of supported metal single atoms. *Nano Res.* **2022**, *15*, 1838–1844.

[39] Li, R.; Yan, X. Y.; Liu, M.; Zhao, Q. K.; Du, J.; Tan, X. X.; Ba, J. W.; Zeng, R. G.; Luo, W. H.; Xu, J. S. Cathodic corrosion as a facile and universal method for scalable preparation of powdery single atom electrocatalysts. *Nano Res.* **2024**, *17*, 4943–4950.

[40] Ferrari, A. C.; Meyer, J. C.; Scardaci, V.; Casiraghi, C.; Lazzeri, M.; Mauri, F.; Piscanec, S.; Jiang, D.; Novoselov, K. S.; Roth, S. et al. Raman spectrum of graphene and graphene layers. *Phys. Rev. Lett.* **2006**, *97*, 187401.

[41] Xu, J. S.; Li, R.; Zeng, R. G.; Yan, X. Y.; Zhao, Q. K.; Ba, J. W.; Luo, W. H.; Meng, D. Q. Platinum single atoms supported on nanoarray-structured nitrogen-doped graphite foil with enhanced catalytic performance for hydrogen evolution reaction. *ACS Appl. Mater. Interfaces* **2020**, *12*, 38106–38112.

[42] Ouyang, B.; Zhang, Y. Q.; Wang, Y.; Zhang, Z.; Fan, H. J.; Rawat, R. S. Plasma surface functionalization induces nanostructuring and nitrogen-doping in carbon cloth with enhanced energy storage performance. *J. Mater. Chem. A* **2016**, *4*, 17801–17808.

[43] Liu, Z. J.; Zhao, Z. H.; Wang, Y. Y.; Dou, S.; Yan, D. F.; Liu, D. D.; Xia, Z. H.; Wang, S. Y. *In situ* exfoliated, edge-rich, oxygen-functionalized graphene from carbon fibers for oxygen electrocatalysis. *Adv. Mater.* **2017**, *29*, 1606207.

[44] Xu, J. S.; Li, R.; Yan, X. Y.; Zhao, Q. K.; Zeng, R. G.; Ba, J. W.; Pan, Q. F.; Xiang, X.; Meng, D. Q. Platinum single atom catalysts for hydrogen isotope separation during hydrogen evolution reaction. *Nano Res.* **2022**, *15*, 3952–3958.

[45] Zhao, Q. P.; Shi, W. X.; Zhang, J. W.; Tian, Z. Y.; Zhang, Z. M.; Zhang, P.; Wang, Y.; Qiao, S. Z.; Lu, T. B. Photo-induced synthesis of heteronuclear dual-atom catalysts. *Nat. Synth.* **2024**, *3*, 497–506.

[46] Mekkering, M. J.; Laan, P. C. M.; Troglia, A.; Bliem, R.; Kizilkaya, A. C.; Rothenberg, G.; Yan, N. Bottom-up synthesis of platinum dual-atom catalysts on cerium oxide. *ACS Catal.* **2024**, *14*, 9850–9859.

[47] Tian, S. B.; Wang, B. X.; Gong, W. B.; He, Z. Z.; Xu, Q.; Chen, W. X.; Zhang, Q. H.; Zhu, Y. Q.; Yang, J. R.; Fu, Q. et al. Dual-atom Pt heterogeneous catalyst with excellent catalytic performances for the selective hydrogenation and epoxidation. *Nat. Commun.* **2021**, *12*, 3181.

[48] Wang, K. Y.; Chen, Y.; Liu, Y. B.; Zhang, H.; Shen, Y. X.; Pu, Z. Y.; Qiu, H. L.; Li, Y. M. Plasma boosted N, P, O co-doped carbon microspheres for high performance Zn ion hybrid supercapacitors. *J. Alloys Compd.* **2022**, *901*, 163588.

[49] Zhong, R.; Lu, X. S.; Zheng, F.; Zhang, J. L.; Hong, R. Y. Effect of carrier gas on nitrogen-doped graphene in AC rotating arc plasma. *J. Mater. Sci.* **2023**, *58*, 8742–8756.

[50] Evazzade, I.; Zagalskaya, A.; Alexandrov, V. Revealing elusive intermediates of platinum cathodic corrosion through DFT simulations. *J. Phys. Chem. Lett.* **2022**, *13*, 3047–3052.

[51] Liu, Z.; Höfft, O.; Gödde, A. S.; Endres, F. *In situ* electrochemical XPS monitoring of the formation of anionic gold species by cathodic corrosion of a gold electrode in an ionic liquid. *J. Phys. Chem. C* **2021**, *125*, 26793–26800.

[52] Elnagar, M. M.; Kibler, L. A.; Jacob, T. Metal deposition and electrocatalysis for elucidating structural changes of gold electrodes during cathodic corrosion. *Green Chem.* **2023**, *25*, 6238–6252.

[53] Zhang, J.; Yu, A. M.; Sun, C. H. Computational exploration of dual atom catalysts loaded on defective graphene for oxygen reduction reaction. *Appl. Surf. Sci.* **2022**, *605*, 154534.

[54] Ding, J. Y.; Peng, Z. M.; Wang, Z. W.; Zeng, C. H.; Feng, Y. H.; Yang, M. S.; Hu, G.; Luo, J.; Liu, X. J. Phosphorus-tungsten dual-doping boosts acidic overall seawater splitting performance over RuO_x nanocrystals. *J. Mater. Chem. A* **2024**, *12*, 28023–28031.

[55] Lu, Z. S.; Yang, H.; Liu, Q.; Luo, J.; Feng, L. G.; Chu, L.; Liu, X. J. Nb_2AlC MAX nanosheets supported Ru nanocrystals as efficient catalysts for boosting pH-universal hydrogen production. *Small* **2024**, *20*, 2305434.

[56] Liu, W. J.; Liu, W. X.; Hou, T.; Ding, J. Y.; Wang, Z. G.; Yin, R. L.; San, X.; Feng, L. G.; Luo, J.; Liu, X. J. Coupling Co–Ni phosphides for energy-saving alkaline seawater splitting. *Nano Res.* **2024**, *17*, 4797–4806.

[57] Chao, T. T.; Luo, X.; Chen, W. X.; Jiang, B.; Ge, J. J.; Lin, Y.; Wu, G.; Wang, X. Q.; Hu, Y. M.; Zhuang, Z. B. et al. Atomically dispersed copper-platinum dual sites alloyed with palladium nanorings catalyze the hydrogen evolution reaction. *Angew. Chem., Int. Ed.* **2017**, *56*, 16047–16051.

[58] Da, Y. M.; Tian, Z. L.; Jiang, R.; Liu, Y.; Lian, X.; Xi, S. B.; Shi, Y.; Wang, Y. P.; Lu, H. T.; Cui, B. H. et al. Dual Pt–Ni atoms dispersed on N-doped carbon nanostructure with novel (NiPt)-N_4C_2 configurations for synergistic electrocatalytic hydrogen evolution reaction. *Sci. China Mater.* **2023**, *66*, 1389–1397.

[59] Li, S.; Yu, J.; Liu, Q.; Liu, J. Y.; Song, D. L.; Zhang, H. S.; Li, R. M.; Zhang, Y.; Wang, J. Preparation of carbon sponge loaded NiPt dual-metal single atom as self-supporting electrode based on inkjet printing technology for efficient hydrogen evolution. *Carbon* **2023**, *215*, 118456.

[60] Ma, M. Y.; Xia, W.; Guo, X. Y.; Liu, W. H.; Cao, D.; Cheng, D. J. Constructing Ni_3Se_2-nanoisland-confined Pt_1Mo_1 dual-atom catalyst for efficient hydrogen evolution in basic media. *Small Struct.* **2024**, *5*, 2300284.

[61] Zhang, L.; Si, R. T.; Liu, H. S.; Chen, N.; Wang, Q.; Adair, K.; Wang, Z. Q.; Chen, J. T.; Song, Z. X.; Li, J. J. et al. Atomic layer deposited Pt–Ru dual-metal dimers and identifying their active sites for hydrogen evolution reaction. *Nat. Commun.* **2019**, *10*, 4936.

[62] Zhang, L. Z.; Jia, Y.; Liu, H. L.; Zhuang, L. Z.; Yan, X. C.; Lang, C. G.; Wang, X.; Yang, D. J.; Huang, K. K.; Feng, S. H. et al. Charge polarization from atomic metals on adjacent graphitic layers for enhancing the hydrogen evolution reaction. *Angew. Chem., Int. Ed.* **2019**, *58*, 9404–9408.

[63] Zhao, W. K.; Luo, C.; Lin, Y.; Wang, G. B.; Chen, H. M.; Kuang, P. Y.; Yu, J. G. Pt–Ru dimer electrocatalyst with electron redistribution for hydrogen evolution reaction. *ACS Catal.* **2022**, *12*, 5540–5548.

[64] Sher Shah, M. S. A.; Jang, G. Y.; Zhang, K.; Park, J. H. Transition metal carbide-based nanostructures for electrochemical hydrogen and oxygen evolution reactions. *EcoEnergy* **2023**, *1*, 344–374.